Research Square

Preprints are preliminary reports that have not undergone peer review.
They should not be considered conclusive, used to inform clinical practice,
or referenced by the media as validated information.

Non-Contact with Photochromism Strong-Coupling Modulation for a Miniaturized Computational Spectrometer

Fan Wang

11205@buaa.edu.cn

Beihang University https://orcid.org/0000-0001-7403-3305

Shuang Zhang

Beihang University

Menghan Tian

Beihang University

Zina Zhao

Beihang University

Zelin Lu

Beihang University

Xiaolan Zhong

Beihang University https://orcid.org/0000-0003-4819-0416

Article

Keywords: computational spectrometer, Fabry-Pérot cavity, photochromic, strong coupling

Posted Date: November 10th, 2026

DOI: https://doi.org/10.21203/rs.3.rs-11474805/v1

License: This work is licensed under a Creative Commons Attribution 4.0 International License.
Read Full License

Additional Declarations: There is no conflict of interest

Abstract

Miniaturized computational spectrometers capable of high-resolution spectral measurement are increasingly in demand for on-chip and portable systems. Dynamic modulation can improve spectral resolution by increasing the number and diversity of spectral responses without enlarging the filter footprint. However, existing electrical and thermal modulation schemes often require complex electrode structures and multistep fabrication processes, increasing device complexity and limiting integration. Developing a non-contact modulation strategy that simplifies device architecture and eliminates complex electrodes is therefore key to realizing lightweight, highly integrated spectrometers. Here, we exploit strong coupling between photochromic molecules and a Fabry–Pérot cavity mode to achieve non-contact dynamic modulate of the filter's transmission spectrum, enriching the spectral sampling information and thereby improving the resolution of spectral reconstruction. With optical modulation, the proposed spectrometer reduces the mean FWHM reconstruction error from 0.50 nm to 0.27 nm and resolves spectral features with an FWHM of 3 nm across 400–700 nm. More importantly, we verified the filter's spatially selective modulation capability. By independently tuning the strong-coupling response in different filter unit through localized illumination, diverse spectral response channels can be dynamically constructed. Even with only four filter units, the system enables spectral reconstruction with good resolution. This non-contact dynamic modulation strategy requires neither structural modification nor complex electrical driving and supports spatially selective control for on-demand spectral channel configuration, enabling compact, low-cost, and reconfigurable spectrometers for on-chip integration, portable sensing, and spectral analysis across diverse applications.

Introduction

Miniaturized spectrometers, owing to their compact size, light weight, and ease of integration, have demonstrated significant application potential in mobile sensing, wearable monitoring, and space exploration[1–6]. As an important approach to miniaturizing spectrometers, computational spectrometers can reach submillimeter-scale footprints by integrating computational approaches with advanced materials or nanostructures, offering a promising platform for high-performance, low-cost, and highly integrated on-chip spectroscopy. They typically adopt metasurfaces[7], photonic crystals[8,9], quantum dot arrays[10–12], Fabry–Pérot (FP) cavities[13–15], two-dimensional (2D) materials[16–18], perovskite[19], and semiconductors[20] as spectral encoding components. Each spectral response unit exhibits distinct spectral characteristics, which enable the incident light to be encoded and subsequently decoded through reconstruction algorithms to recover unknown spectra.

To achieve high-resolution spectral reconstruction over a broad spectral bandwidth, typically requires a sufficient number of spectral response units with distinct responses characteristics to provide diverse, weakly correlated sampling information. When device dimensions are constrained, dynamically tuning the spectral responses of optical filters can increase the number of effective sampling channels and thereby enhance spectral reconstruction, such as liquid crystals[21–23], electrochromic devices[24,25], VO_2[26],

and lithium niobate[27]. However, these approaches largely rely on contact-based electrical actuation or thermal tuning, with complex electrode configurations and multistep deposition processes that increase the difficulty of device design and fabrication while constraining further improvements in device integration[14,28]. Developing a non-contact modulation strategy that eliminates complex electrode configurations and simplifies device architecture is therefore important for realizing lightweight, highly integrated broadband spectrometers.

In this work, we propose a non-contact modulation strategy based on photochromically tunable strong coupling. By integrating photochromic molecules into Fabry–Pérot (F–P) microcavities, we construct a strongly coupled molecule–microcavity filter array, and by dynamically tuning the coupling strength between the molecules and the cavity modes using ultraviolet light, thereby enabling dynamic modulation of the transmission spectra over a broad wavelength range. The strongly coupled photochromic on-chip computational spectrometer (PCOS) acquires diverse spectral sampling information through dynamic transmission responses under different optical conditions, enabling high-quality reconstruction of monochromatic and complex spectra over the 400–700 nm wavelength range and resolving dual-peak spectra with a peak separation of just 4 nm. Further investigations show that the system maintains good broadband spectral detection and reconstruction performance using only four filter units. This non-contact dynamic spectral modulation strategy effectively increases the number of sampling channels and broadens the spectral response range within a limited device footprint. By enabling on-demand spectral channel configuration through spatially selective control, it enhances the flexibility of spectral reconstruction and offers a new pathway toward lightweight, highly integrated miniaturized spectrometers.

Results

We exploit the strong coupling between photochromic materials and F-P microcavities to develop a non-contact computational spectrometer based on a strongly coupled photochromic FP-cavity filter array, whose spectral response can be dynamically tuned by external light irradiation. Photochromism is a phenomenon in which the color, transmission spectrum, and other optical properties of a material undergo reversible changes upon exposure to optical irradiation[29]. Leveraging this effect, external optical stimulation alone can enable the same filter unit to generate distinct spectral responses under different irradiation states, thereby increasing the number of spectral samples without adding physical units. However, the spectral modulation range of photochromic materials alone is typically limited to their intrinsic absorption bands, making broadband spectral encoding challenging and consequently restricting the wavelength range of spectral reconstruction. To overcome this limitation, we incorporate photochromic molecules into Fabry–Pérot (FP) microcavities and exploit strong coupling between the molecular absorption transition and the cavity resonance mode to broaden the spectral modulation range. When the two are resonant and the coupling strength exceeds the system losses, the cavity photons and molecular excited states form hybrid light–matter states, causing the original cavity mode to split into upper and lower polariton branches, with their energy separation determined by the coupling

strength[30–33]. Thus, light-induced changes in the molecular state enable dynamic tuning of the molecule–cavity coupling strength and polariton resonance positions, generating diverse transmission spectra beyond the intrinsic molecular absorption band and providing richer sampling information for broadband spectral reconstruction.

The photochromic filter array consists of two silver (Ag) films with different spiropyran (SPI) photochromic molecular layers of different thicknesses embedded between them, the schematic as shown in Fig. 1a. The SPI molecules exhibit no pronounced absorption in the visible range, therefore, the transmission spectrum of the system displays only the intrinsic F-P cavity modes. Under ultraviolet (UV) irradiation at 365 nm, the C–O bond in SPI cleaves, driving a conformational transformation from a twisted to a planar structure and converting the transparent SPI into the absorbing Merocyanine (MC) form[34,35], as shown in Fig. 1b. As the absorption of the MC state increases, the coupling strength between the molecules and the F-P cavity increases accordingly. When the molecular absorption transition is resonant with the cavity mode and the coupling strength exceeds the system losses, the system enters the strong-coupling regime. Consequently, the initial single transmission peak splits into two distinct peaks corresponding to the upper and lower polariton branches, which arise from the hybridization of molecular excitations and cavity photons. The absorption spectra for SPI molecules converting to the MC state under UV irradiation is presented in Fig. S1. The molecule reverts to the SPI state under intense visible light. More details of the strong coupling principles can be found in Supplementary Information S2. Variations in the molecular layer thickness alter the F-P cavity length, resulting in distinct transmission spectra for different array units. The photochromic filter array, which has a size of 1cm × 1cm, is integrated directly on top of the CMOS sensor to form the PCOS, as shown in Fig. 1c. The transmission spectra exhibited by each filter array unit under different UV irradiation times collectively constitute the response function. By combining this pre-calibrated response function with the unknown transmission intensities measured at different UV irradiation times, the unknown spectrum can be reconstructed with algorithmic processing. During operation, the incident spectrum $S(\lambda)$ is encoded by the filter array's spectral response $T_i(t_j, \lambda)$ under distinct irradiation states t_j as

$$\int_{\lambda_{min}}^{\lambda_{max}} S(\lambda) \bullet T_i(t_j, \lambda) \bullet \eta(\lambda) = I_i^j (i = 1, 2, \ldots n) \quad (1)$$

Where λ_{min} and λ_{max} define the wavelength range of the spectrometer, and $\eta(\lambda)$ is the quantum efficiency of the CMOS sensor. The $j(j = 1, 2, 3)$ denotes different detection modes, which correspond to exposure times of 0 s; 0 s, 2 s; and 0 s, 2 s, 6s sampling illumination, respectively. The measured intensity I_i^j at j detection modes, represents the integral of $S(\lambda)\ T_i(t_j, \lambda)\ \eta(\lambda)$, determined by the photocurrents of the CMOS sensor.

To verify that photochromism can modulate the molecule–microcavity coupling strength, we measured the spectral responses of the F-P microcavity at different UV irradiation times. Figure 2a is the schematic diagram of the F-P microcavity that contains an SPI molecule layer, where the SPI molecule can transfer to the MC state under UV irradiation. As the UV irradiation time increases, SPI molecules are gradually converted into the MC state, and the molecular absorption intensity continuously increases, driving the

system from the weak-coupling regime to the strong-coupling regime, as shown in Fig. 2b. When the coupling strength exceeds the average dissipation rate of the system, the system enters the strong-coupling regime, and the original single-peak transmission spectrum symmetrically splits into two distinct peaks. After the UV irradiation is stopped, the molecules undergo bleaching and return to their initial state, and the system's transmission spectrum consequently returns to a single-peak profile. Figure 2c shows the angle-resolved transmission spectra (TE polarization) of the photochromic microcavity. The system exhibits only the cavity-mode resonance peak when the molecules are in the SPI state, with the cavity dispersion showing a single-branch profile and the resonance energy increasing with the incidence angle. After the molecules transfer into the MC state (Fig. 2d), the dispersion curve splits into the upper and lower polariton branches, indicating that the system enters the strong-coupling regime. At zero detuning, where the bare cavity mode is resonant with the molecular transition, a Rabi splitting of 790 meV is obtained. The angle-dependent transmission spectra of the photochromic F-P cavity are shown in Fig.S3.

The capabilities of a computational spectrometer are determined by the diversity of its wavelength-dependent optical response. To establish spectral sampling channels with distinct response characteristics, we tuned the resonance conditions of F–P microcavities by varying the molecular layer thickness and designed a photochromic filter array comprising nine microcavity units with different molecular layer thicknesses. Figure 3a shows the measured transmission spectra of the filter array. With the thickness of the filter units increasing from 115 nm to 167 nm, the transmission peaks exhibit a redshift. Figure 3b shows the distribution of the filter-array units in the CIELAB color space, revealing a broad color-rendering range that covers the red, yellow, blue, and green regions. Furthermore, the transmission spectra of the filter-array units were measured after the molecules were converted to the MC state by 6s of UV irradiation, as shown in Fig. 3c. The transmission spectra of the individual units exhibit pronounced differences due to the different coupling conditions between the cavity modes and the molecular transition. Therefore, by varying the cavity length and UV irradiation duration, the spectral response can be tuned in both intensity and peak position, thereby effectively increasing the number of available spectral channels. The transmission spectra of each filter unit at multiple intermediate states are shown in Fig.S4. The correlation coefficient heatmap of spectral responses under different irradiation times indicates that the 27 channels of the filter array exhibit low mutual correlations, as shown in Fig. 3d. The average correlation coefficient of the filter array is 0.31, indicating low correlations among the spectral response channels, which reduces redundancy and crosstalk between the sampling channels and is beneficial for improving the stability and accuracy of spectral reconstruction. Further details regarding the Pearson correlation coefficient are provided in Supplementary Information S5.

To evaluate the spectral reconstruction performance of PCOS, we used a filter array comprising nine units to reconstruct unknown spectra. Figure 4a shows the reconstructed spectra of monochromatic light at 452nm under three working modes (m = 1, 2, and 3). Here, m denotes different working modes: m = 1 indicates the mode with ‘0 s’ of UV irradiation time, m = 2 indicates the mode with ‘0 s’ and ‘2 s’ of UV irradiation time, m = 3 indicates the mode with ‘0 s’, ‘2 s’, and ’6 s’ of UV irradiation time. As the number of UV irradiation states used for spectral sampling increases, the reconstructed spectra

demonstrate higher fidelity, showing good agreement with the reference spectra measured by a commercial spectrometer (FLS1000 EDINBURGH), particularly for m = 3. Seven monochromatic input spectra with a bandwidth of 3 nm and peak wavelengths spanning 400–700 nm were reconstructed under m = 3, as shown in Fig. 4b. The reconstructed spectra exhibit excellent agreement with the reference spectra. Peak wavelength difference ($\Delta\lambda$) and full width at half-maximum (FWHM) represent two essential metrics for the accuracy and resolution of computational spectrometers. Figure 4c shows $\Delta\lambda$ and the FWHM error between the reconstructed spectra and reference spectra. As the working modes vary from m = 1 to m = 3 and the spectra channels increase (9, 18, 27 for m = 1, 2, 3, respectively), leading to the average $\Delta\lambda$ reduced from 0.46 nm (m = 1) to 0.20 nm (m = 2), 0.03 nm (m = 3) and the FWHM error reduced from 0.5 nm (m = 1) to 0.42 nm (m = 2), 0.27 nm (m = 3). In addition, we measured a complex double-peak spectrum containing two closely spaced peaks separated by only 4 nm at approximately 513 nm. The results demonstrate that the spectrometer can effectively resolve two peaks separated by 4 nm. The reconstructions for m = 1 and 2 exhibit more pronounced deviations (Fig. 4d, e), and the reconstruction of the m = 3 mode (Fig. 4f) shows strong agreement with the reference spectra, confirming the PCOS's ability to distinguish closely spaced peaks. To quantitatively evaluate the spectral reconstruction performance of the PCOS, we further calculate the mean squared error (MSE) between the reconstructed and reference spectra. Further details regarding the MSE are provided in Supplementary Information S6. The MSE values for the reconstructed spectra under the three working modes (m = 1, 2, and 3) are 0.09, 0.01, and 0.01, respectively (inset in Fig. 4f). The gradual decrease in MSE with increasing the m demonstrates that increasing the number of spectral samples effectively improves the ability to resolve closely spaced peaks. Additional reconstruction of the spectra with two mixed peaks is given in Fig.S7.

We further evaluated the reconstruction capability of the PCOS for narrowband, broadband, and asymmetric-profile spectra using a filter array comprising nine units. For a relatively narrowband spectrum from a red LED (with a peak at 618 nm and a FWHM of ~ 30 nm), the PCOS accurately reconstructed the full spectral profile under three working modes (Fig. 5a, b, c). As additional UV irradiation states were incorporated into the reconstruction, the reconstructed peak wavelength approached the reference peak, shifting from 610 nm at m = 1 mode to 618 nm at m = 2 mode and 617 nm at m = 3 mode, while the MSE for the m = 3 mode reached 0.003. The continuous broadband spectra were generated by a xenon lamp combined with a 400 nm long-pass filter and a 550 nm short-pass filter. To modulate the intensity distribution within this wavelength range, additional color filters were inserted into the optical path, yielding distinct symmetric and asymmetric spectral profiles (Fig. 5d-i). For symmetric profiles, in the m = 1 mode, the reconstructed spectra exhibit a pronounced mismatch with the reference, which fundamentally stems from the limitations of low-dimensional spectral encoding. As the number of spectral channels doubles and triples, the reconstruction quality improves from poor to acceptable, and finally to excellent. Specifically, the reconstructed spectra show noticeable enhancement in the m = 2 mode (Fig. 5e) and achieve excellent agreement with the reference in the m = 3 mode (Fig. 5f). Correspondingly, the MSE values decrease from 0.04 to 0.03 and 0.02, as shown in the inset of Fig. 5f. For asymmetric profiles, a similar progressive trend from poor to excellent is observed as

the illumination time extends. In the m = 1 mode, the features of the reconstructed spectra are entirely inconsistent with the reference. With the increase of spectral channels, the consistency between the reconstructed and reference spectra demonstrates a clear upward trend, evolving from a moderate reconstruction in the m = 2 mode (Fig. 5h) to an optimal reconstruction in the m = 3 mode (Fig. 5i). The MSE values are reduced from 0.05 to 0.02 and 0.02 for the inset of Fig. 5i, for m = 1, 2, 3, respectively. This enhancement arises from photoinduced modulation of the spectral responses of the filter array, which increases the number of effective spectral sampling channels and thereby significantly enhances the spectral resolution. The light-modulation strategy offers a flexible operating mode tailored to the complexity of the target spectra. To be specific, adaptive configurations can be implemented based on the structural features of the spectra in distinct application scenarios: for relatively simple spectral profiles (e.g., narrowband or sparse spectra), the operational workflow can be simplified by avoiding light modulation (m = 1) to achieve high temporal efficiency; conversely, when facing complex spectral profiles with intricate features or broad bands, prolonged illumination modulation (e.g., increasing to m = 2, m = 3, or higher) is preferred to enrich the spectral encoding dimensions and ensure high-fidelity reconstruction.

To verify the spatial selectivity of photochromic modulation and assess spectral reconstruction with a limited number of filter units, we reduced the filter array to just four units and quantitatively evaluated the spectral reconstruction resolution in this configuration, as shown in Fig. 6. The reconstruction accuracy was evaluated using three characteristic monochromatic inputs centered at 478 nm, 523 nm, and 642 nm, respectively (Fig. 6a-c). In the m = 1 mode, due to the severely limited number of spectral channels, the wavelength resolution capability of the system is insufficient. This leads to a large deviation between the reconstructed and reference spectra, primarily manifested as peak shifts and the appearance of spurious peaks. In the m = 2 mode, the resolution of the reconstructed spectrum was improved. Ultimately, in the m = 3 mode, the spectral reconstruction quality reaches its optimum, with the reconstructed spectra exhibiting high fidelity and consistency with the reference spectra. A decrease in the number of spectral units will impact the reconstruction quality of double-peaked spectra. The PCOS with four filter units can only resolve double peaks separated by 9 nm with the aid of photochromism, as shown in Fig. 6d. We further quantify them by using MSE, as shown in the inset of Fig. 6d-iii. The MSE values for the three modes are consistently within 0.06. Additionally, we successfully reconstructed a narrowband spectrum with only four filter units, as shown in Fig.S8. Figure 6e shows the reconstruction of broadband spectra with asymmetric profiles. In modes m = 1 and m = 2, the reconstructed spectra show noticeable deviations from the reference spectra. As the number of irradiation states used for spectral sampling increases, the resolution gradually improves, and the MSE continuously decreases, from 0.05 (m = 1) to 0.02 (m = 2) and 0.02 (m = 3). Even with only four filter units, photochromic modulation can still improve the spectrum resolution in reconstructing complex spectra. This indicates that photochromic modulation can expand the number of effective spectral sampling channels without increasing the number of physical units, thereby partially compensating for the loss of sampling information associated with fewer filter units. Additional broadband spectral reconstruction results for the six filter units PCOS configuration are detailed in Fig.S9.

Discussion

In conclusion, we propose an electrodeless and non-contact dynamic optical modulation strategy for miniaturized spectrometers. This strategy uses external light irradiation to induce the reversible photoinduced spectral transformation in photochromic molecules, the strong-coupling state between molecular absorption transitions and Fabry–Pérot cavity modes can be dynamically regulated to reconfigure the spectral responses of the filter array. This expands the number of effective spectral sampling channels and enhances response diversity without increasing the number of physical filter units, thereby improving spectral reconstruction fidelity over the wavelength range of 400–700 nm. The average FWHM reconstruction deviation for monochromatic spectra decreases from 0.5 nm to 0.27 nm as the sample number increased with external light modulation. Furthermore, PCOS maintains great broadband spectral reconstruction performance even when the number of physical filter units is reduced to only four, demonstrating that photochromic modulation can expand the effective sampling channels and thereby partially compensate for the limitations imposed by a restricted number of physical sampling units. Further optimization of the photochromic on-chip spectrometer holds significant potential for further reducing the device footprint and extending the spectral operating range. These performance improvements can be realized by engineering the spectral response of the photochromic materials through the introduction of additional photoactive units, molecular modifications, or dopants. For instance, donor–acceptor Stenhouse adducts (DASAs), combined with suitable organic chromophores, provide tunable photochromic responses across the UV–visible region through rational control of molecular composition, mixing ratio, and concentration[33]. This approach could be further extended toward the near-infrared by employing photochromic molecules such as diarylethene (DAE) molecules with near-infrared absorption[36]. In parallel, rational matching between the molecular absorption transitions and cavity resonances may provide an additional degree of freedom for tailoring the strong-coupling response and extending the effective spectral modulation bandwidth. The synergy between photochromism and strong coupling therefore provides not only a non-contact means of dynamically increasing spectral sampling channels, but also a route to overcoming the intrinsic spectral-range limitation of individual photochromic materials. This approach offers a promising pathway toward compact, low-cost, broadband, and high-performance on-chip optical analysis systems.

Materials and methods

The photochromic spiropyran (SPI) (1′,3′-dihydro-1′,3′,3′-trimethyl-6-nitrospiro[2*H*-1-benzopyran − 2, 2′-(2H) indole]) molecule and polymethyl methacrylate (PMMA, average M_w, ~ 120,000) were purchased from Sigma-Aldrich. The toluene was purchased from Beijing Eastern Noble Co., Ltd. (Beijing, China). All chemicals and reagents were purchased from commercial suppliers and used as received without further purification.

Fabrication and characterization of photochromic F-P microcavity filter array

The device fabrication process includes three steps. To fabricate the photochromic F-P microcavity filter array, the PET substrates were cleaned by sequential sonication in acetone, methanol, and deionized water for 15 minutes each, then dried in an oven at 60°C. A 30-nm-thick Ag film layer was deposited on the cleaned PET by pulsed direct current (DC) reactive magnetron sputtering (ZDF-5227, Changzhou Hongming Instrument Technology Co., Ltd., China). To prepare the middle photochromic molecular layer of the cavity, a PMMA-toluene solution (2.5wt% PMMA, M_ω = 120 000) was thoroughly mixed with SPI to achieve an SPI-to-PMMA weight ratio of 3:2. The resulting mixture was spin-coated onto the prefabricated Ag film for 40 s at various rotation speeds. The spinning velocity was systematically varied to precisely modulate the thickness of the cavity, thereby tuning the empty-cavity resonance wavelength. The optical cavity was subsequently enclosed by sputtering an additional 30-nm Ag film. The deposition process was executed under a sputtering pressure of 0.8 Pa and a power of 30 W for a duration of 2 min. The transmittance of the sample was measured by an ultraviolet-visible spectrometer (TU-1810, PERSEE). The narrowband spectrum is provided by a red LED (GCI-060401, Daheng Optics).

Calibration and reconstruction experiments

Calibration process

A 365 nm UV LED (LEM365 JCOPTIX) provides UV irradiation. In the calibration process, the irradiation time was chosen as 0 s, 2 s, and 6 s. The measured intensities of each filter unit are read out from the CMOS camera (acA1920-150um, Basler) to form the spectral response $T_i(t_j, \lambda)$. A tunable quasi-monochromatic spectrum derived from the xenon lamp (FLS1000 EDINBURGH) was used for wavelength-dependent illumination. The FWHM of the monochromatic light is approximately 3 nm, and the wavelength step size is 1 nm. The unknown spectrum of incident light was measured using a commercial spectrometer (FLS1000 EDINBURGH) for reference. The schematic of the optical setup for calibration and measurement of the PCOS is shown in Fig.S10. All measurements were conducted under stable ambient conditions (≈ 20% RH, ≈ 20°C).

Spectrum reconstruction

The reconstruction algorithm for monochromatic light, dual - peak spectra, and narrowband spectra is an adaptive Tikhonov regularization[20,37], which uses a linear combination of Gaussian basis functions to fit the target spectrum. The reconstruction algorithm for broadband spectra is total variation minimization by augmented Lagrangian[38] and the alternating direction algorithm[39].

Declarations

Acknowledgments

This work is supported by the National Natural Science Foundation of China (62505014, 12674454, U23A2048) and the Fundamental Research Funds for the Central Universities. We are grateful to the

Atomic-Scale In Situ Fabrication platform of the Analysis & Testing Center of Beihang University for the facilities and the scientific and technical assistance.

Data availability

The data that support the findings of this study are available from the corresponding authors upon reasonable request.

References

1. Park, J. W. et al. Wearable Hyperspectral Photoplethysmography Allows Continuous Monitoring of Exercise-Induced Hypertension. Adv Sci (Weinh) 12, e2417625 (2025). https://doi.org/10.1002/advs.202417625
2. Bec, K. B., Grabska, J. & Huck, C. W. Principles and Applications of Miniaturized Near-Infrared (NIR) Spectrometers. Chemistry 27, 1514–1532 (2021). https://doi.org/10.1002/chem.202002838
3. Blind, N., Le Coarer, E., Kern, P. & Gousset, S. Spectrographs for astrophotonics. Opt Express 25, 27341–27369 (2017). https://doi.org/10.1364/OE.25.027341
4. Yang, Z., Albrow-Owen, T., Cai, W. & Hasan, T. Miniaturization of optical spectrometers. Science 371 (2021). https://doi.org/10.1126/science.abe0722
5. Wang, X. et al. Exploiting universal nonlocal dispersion in optically active materials for spectro-polarimetric computational imaging. eLight 4 (2024). https://doi.org/10.1186/s43593-024-00078-2
6. Crocombe, R. A. Portable Spectroscopy. Applied Spectroscopy 72, 1701–1751 (2018). https://doi.org/10.1177/0003702818809719
7. Lee, D.-g., Song, G., Lee, C., Lee, C. & Jang, M. Reconstructive spectrometer using double-layer disordered metasurfaces. Science Advances 11, eadv2376 (2025). https://doi.org/doi:10.1126/sciadv.adv2376
8. Zhu, Y., Lei, X., Wang, K. X. & Yu, Z. Compact CMOS spectral sensor for the visible spectrum. Photonics Research 7 (2019). https://doi.org/10.1364/prj.7.000961
9. Wang, Z. et al. Single-shot on-chip spectral sensors based on photonic crystal slabs. Nat Commun 10, 1020 (2019). https://doi.org/10.1038/s41467-019-08994-5
10. Bao, J. & Bawendi, M. G. A colloidal quantum dot spectrometer. Nature 523, 67–70 (2015). https://doi.org/10.1038/nature14576
11. Zhu, X. et al. Broadband perovskite quantum dot spectrometer beyond human visual resolution. Light Sci Appl 9, 73 (2020). https://doi.org/10.1038/s41377-020-0301-4
12. Li, H. et al. A Near-Infrared Miniature Quantum Dot Spectrometer. Advanced Optical Materials 9, 2100376 (2021). https://doi.org/https://doi.org/10.1002/adom.202100376
13. Zhang, Y. et al. Miniature computational spectrometer with a plasmonic nanoparticles-in-cavity microfilter array. Nat Commun 15, 3807 (2024). https://doi.org/10.1038/s41467-024-47487-y

14. Yako, M. et al. Video-rate hyperspectral camera based on a CMOS-compatible random array of Fabry–Pérot filters. Nature Photonics 17, 218–223 (2023). https://doi.org/10.1038/s41566-022-01141-5
15. Wang, S.-W. et al. Concept of a high-resolution miniature spectrometer using an integrated filter array. Opt. Lett. 32, 632–634 (2007). https://doi.org/10.1364/OL.32.000632
16. Du, X. et al. A microspectrometer with dual-signal spectral reconstruction. Nature Electronics 7, 984–990 (2024). https://doi.org/10.1038/s41928-024-01242-9
17. Uddin, M. G. et al. Broadband miniaturized spectrometers with a van der Waals tunnel diode. Nat Commun 15, 571 (2024). https://doi.org/10.1038/s41467-024-44702-8
18. Li, X. et al. Nonlinear memristive computational spectrometer. Light Sci Appl 14, 47 (2025). https://doi.org/10.1038/s41377-024-01703-y
19. Liu, S. et al. A Vertically Bandgap-Cascaded Perovskite Single-Crystal Film Heterojunction for On-Chip Spectral Imaging. Advanced Materials (2026). https://doi.org/10.1002/adma.74281
20. Yang, Z. et al. Single-nanowire spectrometers. Science 365, 1017–1020 (2019). https://doi.org/doi:10.1126/science.aax8814
21. Zhou, Z. et al. Electrically tunable planar liquid-crystal singlets for simultaneous spectrometry and imaging. Light: Science & Applications 13 (2024). https://doi.org/10.1038/s41377-024-01608-w
22. Ni, Y. et al. Computational spectropolarimetry with a tunable liquid crystal metasurface. eLight 2 (2022). https://doi.org/10.1186/s43593-022-00032-0
23. Wu, X. et al. A Multi-Resonant Tunable Fabry-Pérot Cavity for High Throughput Spectral Imaging. Advanced Optical Materials 13 (2024). https://doi.org/10.1002/adom.202402784
24. Tian, M. et al. Miniaturized on-chip spectrometer enabled by electrochromic modulation. Light Sci Appl 13, 278 (2024). https://doi.org/10.1038/s41377-024-01638-4
25. Zhang, X. et al. Multifunctional integrated electrochromic device by p-n conductive polymers for self-powered smart windows and miniaturized spectrometers. Nature Communications 16 (2025). https://doi.org/10.1038/s41467-025-67903-1
26. Guo, T. et al. Miniaturized Hyperspectral Imager Utilizing a Reconfigurable Filter Array for Both High Spatial and Spectral Resolutions. Nano Lett 24, 11156–11162 (2024). https://doi.org/10.1021/acs.nanolett.4c01075
27. Yao, Z., Liu, S., Wang, Y., Yuan, X. & Fang, L. Integrated lithium niobate photonics for sub-ångström snapshot spectroscopy. Nature 646, 567–575 (2025). https://doi.org/10.1038/s41586-025-09591-x
28. You, C. et al. CMOS-compatible reconstructive spectrometers with self-referencing integrated Fabry-Perot resonators. Proc Natl Acad Sci U S A 121, e2403950121 (2024). https://doi.org/10.1073/pnas.2403950121
29. Zhang, J., Zou, Q. & Tian, H. Photochromic Materials: More Than Meets The Eye. Advanced Materials 25, 378–399 (2013). https://doi.org/https://doi.org/10.1002/adma.201201521

30. Hutchison, J. A., Schwartz, T., Genet, C., Devaux, E. & Ebbesen, T. W. Modifying Chemical Landscapes by Coupling to Vacuum Fields. Angewandte Chemie International Edition 51, 1592–1596 (2012). https://doi.org/10.1002/anie.201107033
31. Zeng, H. et al. Control of Photoswitching Kinetics with Strong Light-Matter Coupling in a Cavity. J Am Chem Soc 145, 19655–19661 (2023). https://doi.org/10.1021/jacs.3c04254
32. Lee, I., Melton, S. R., Xu, D. & Delor, M. Controlling Molecular Photoisomerization in Photonic Cavities through Polariton Funneling. Journal of the American Chemical Society 146, 9544–9553 (2024). https://doi.org/10.1021/jacs.3c11292
33. Asamoah, B. O. et al. Optically induced crossover from weak to strong coupling regime between surface plasmon polaritons and photochromic molecules. Optics Express 28 (2020). https://doi.org/10.1364/oe.400359
34. Kortekaas, L. & Browne, W. R. The evolution of spiropyran: fundamentals and progress of an extraordinarily versatile photochrome. Chemical Society Reviews 48, 3406–3424 (2019). https://doi.org/10.1039/c9cs00203k
35. Schwartz, T., Hutchison, J. A., Genet, C. & Ebbesen, T. W. Reversible switching of ultrastrong light-molecule coupling. Phys Rev Lett 106, 196405 (2011). https://doi.org/10.1103/PhysRevLett.106.196405
36. Majumdar, A., Jahan, N. & Thakur, A. Design Strategies for the Construction of Visible-to-NIR Light Triggered Diarylethenes. Chem Asian J 20, e00831 (2025). https://doi.org/10.1002/asia.202500831
37. Yoon, H. H. et al. Miniaturized spectrometers with a tunable van der Waals junction. Science 378, 296–299 (2022). https://doi.org/doi:10.1126/science.add8544
38. Duan, Y. & Huang, W. A fixed-point augmented Lagrangian method for total variation minimization problems. Journal of Visual Communication and Image Representation 24, 1168–1181 (2013). https://doi.org/10.1016/j.jvcir.2013.07.014
39. Li, C., Yin, W., Jiang, H. & Zhang, Y. An efficient augmented Lagrangian method with applications to total variation minimization. Computational Optimization and Applications 56, 507–530 (2013).

Figures

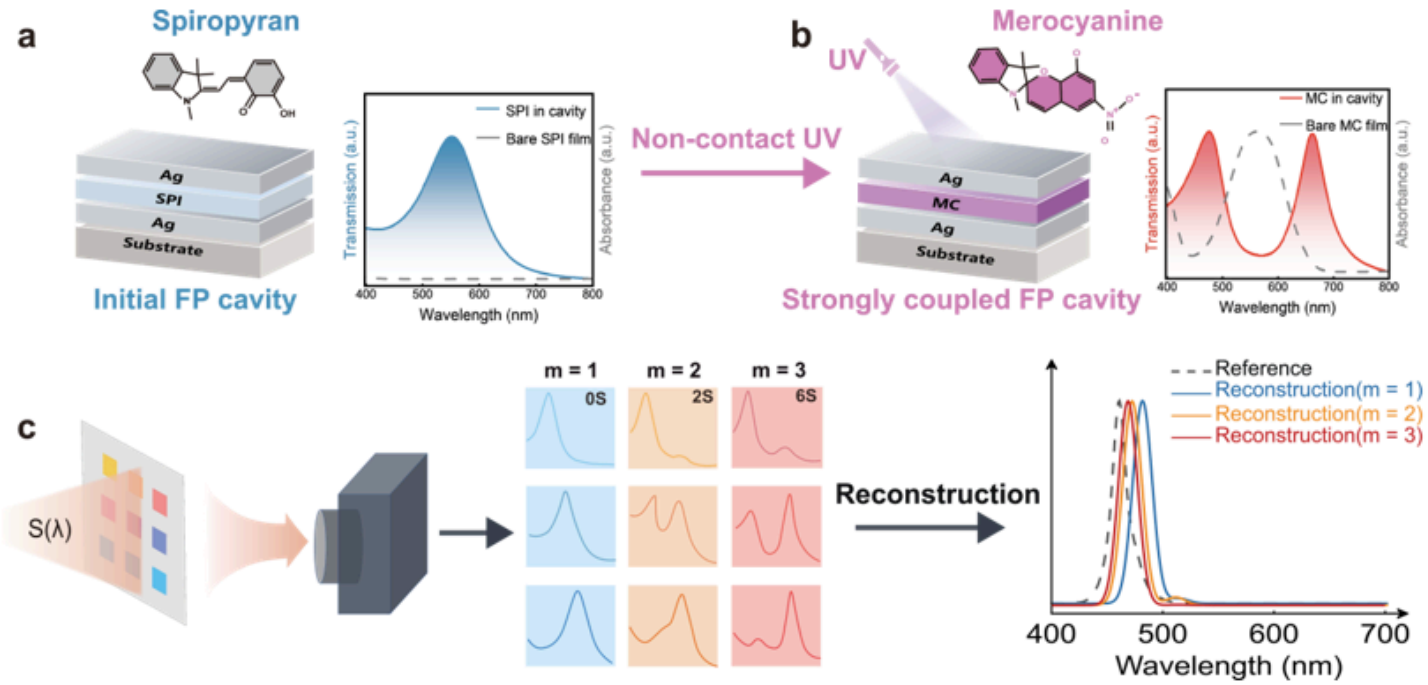


Figure 1

Schematic of the working principle of the strongly coupled photochromic on-chip computational spectrometer (PCOS). (a) Schematic of photochromic molecules within the Fabry–Pérot (FP) microcavity in the spiropyran (SPI) and (b) merocyanine (MC) states, respectively. Absorption spectra for a molecular film in the SPI and MC forms (solid line) are shown in gray. Transmission spectra of the F-P microcavity with the molecules in the SPI (blue line) and MC (red line) forms. (c) Principle of PCOS. The schematic of the transmission spectra corresponding to three different UV irradiation states (0s, 2s, and 6s), and the reconstructed spectra under three conditions of UV irradiation states. Here, m denotes different working modes: m = 1 (blue) indicates the mode with ‘0 s’ of UV irradiation time, m = 2 (orange) indicates the mode with ‘0 s’ and ‘2 s’ of UV irradiation time, m = 3 (red) indicates the mode with ‘0 s’, ‘2 s’, and ’6 s’ of UV irradiation time.

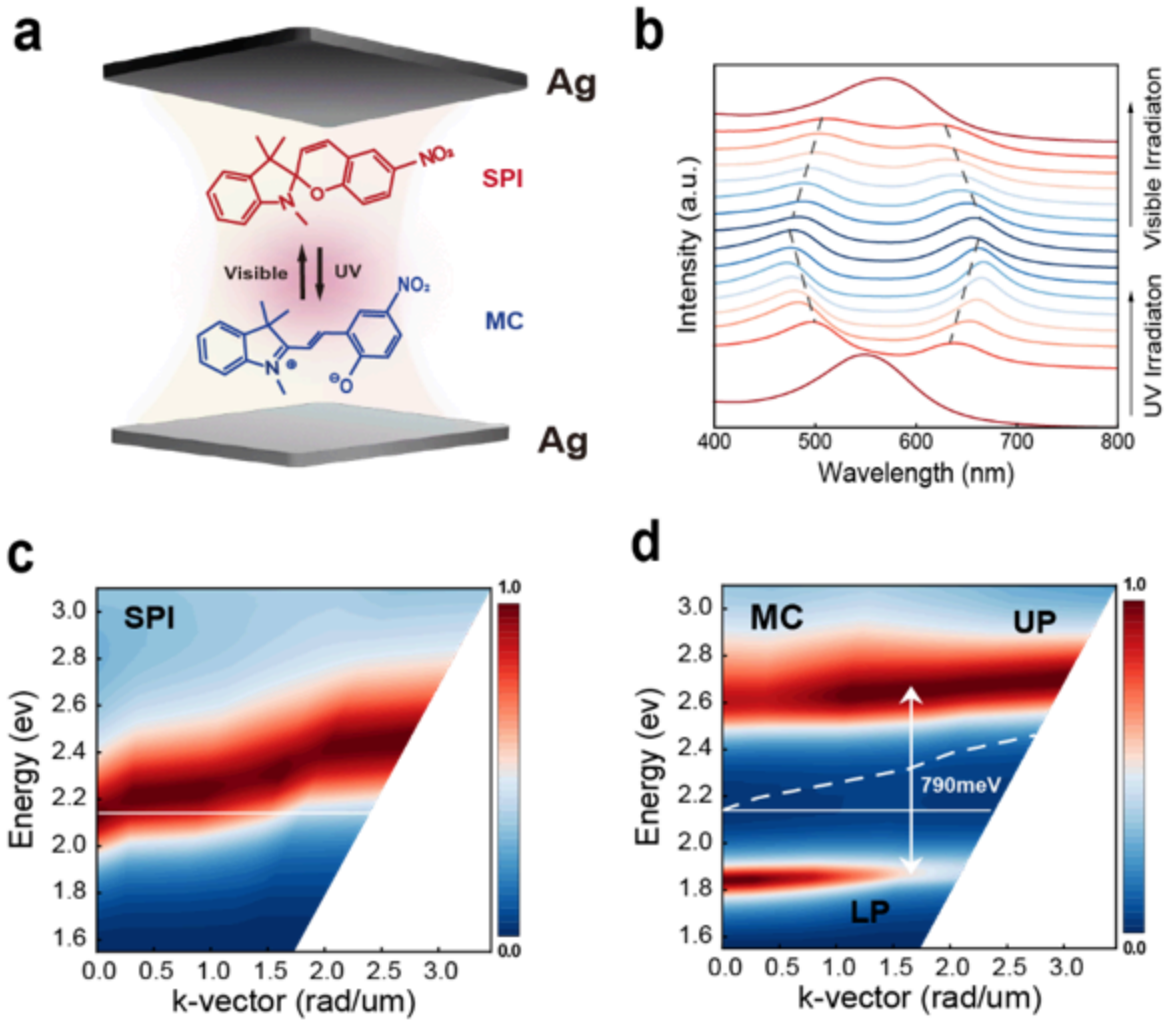


Figure 2

Optical characterization of photochromic F-P microcavities. (a) Schematic of the photochromic F-P microcavity. (b) The transmission spectra of the photochromic filter under different UV irradiation times. (c) Angle-resolved transmission spectra (TE polarization) of the molecules in the SPI state and (d) the MC state.

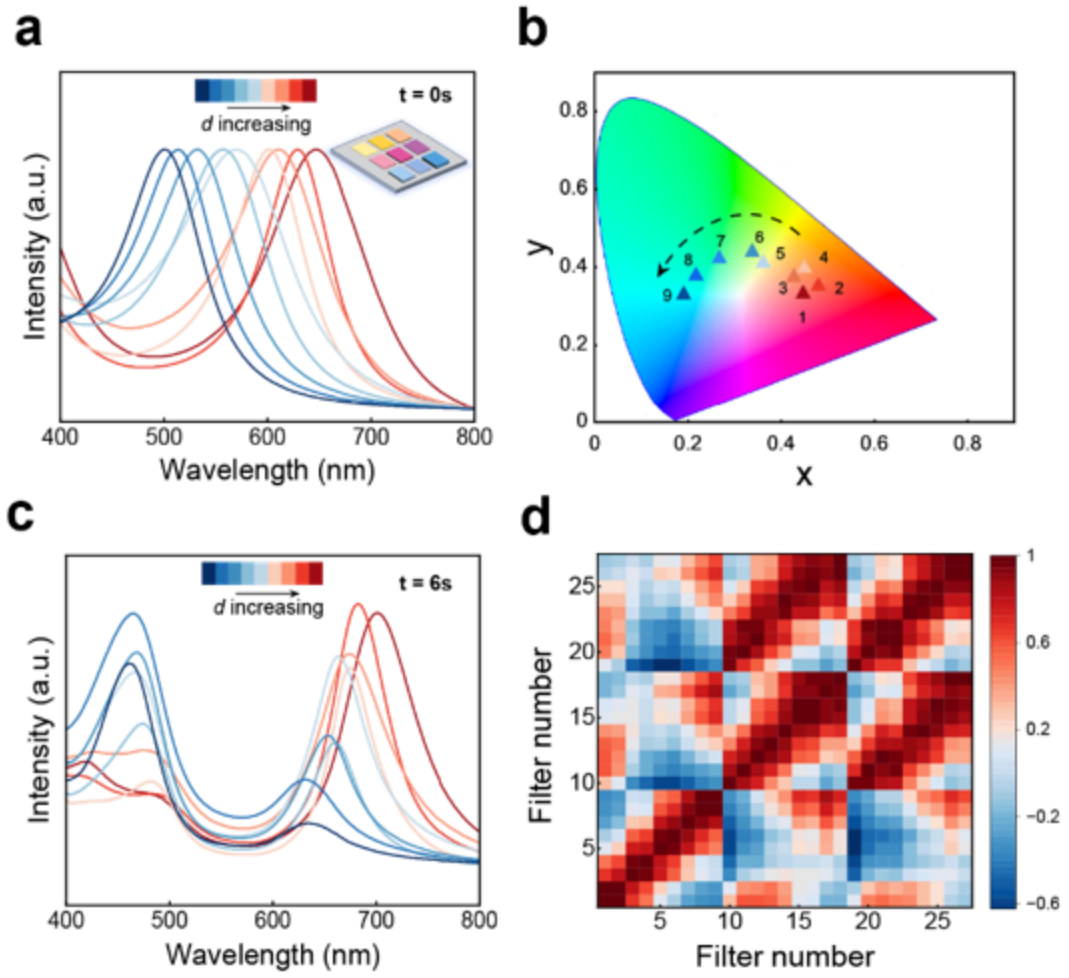


Figure 3

Transmission spectrum of the photochromic filter array. (a) Transmission spectra of a filter array with different SPI molecule layers with varying thicknesses in F-P cavities. (b) The CIELAB color space plots represent the color coordinates of filter array units. (c) Transmission spectra of filter array units under molecules in the MC state. (d) Heatmap of correlation coefficients of the photochromic filter array units.

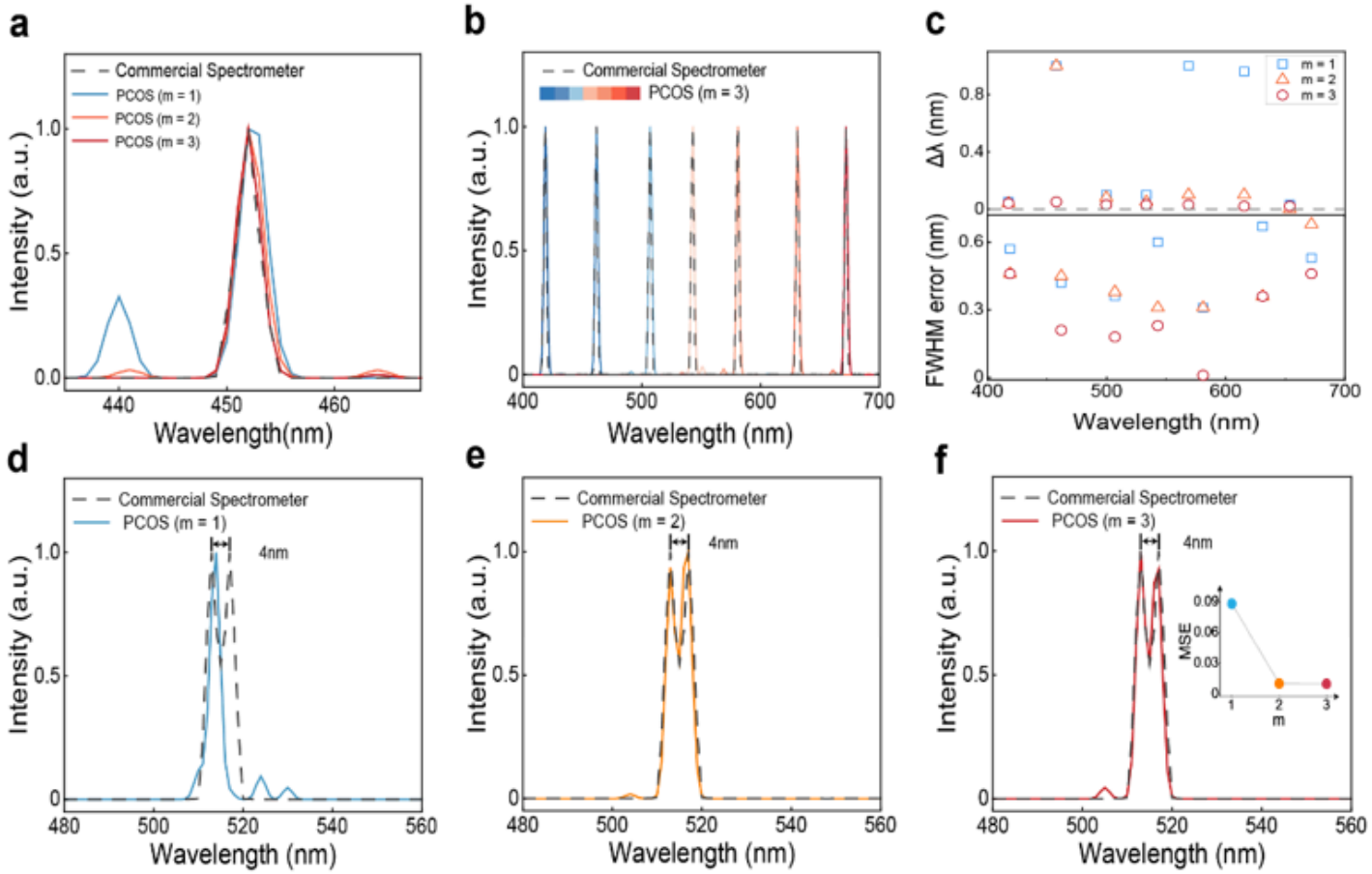


Figure 4

The performance of PCOS under different working modes. (a) Reconstruction of quasi-monochromatic spectra at 452 nm. (b) Spectral reconstruction results for seven single peaks with FWHM of 3 nm over the wavelength range of 400-700 nm under the m = 3 working mode. (c) Peak wavelength difference between reconstructed and reference spectra by a commercial spectrometer (upper panel), and FWHM deviation between reconstructed and reference spectra (lower panel). (d-f) Reconstruction of the spectrum with two mixed peaks of 4 nm under different working modes. The inset of (f) shows the MSE of different modes of m. Here m denotes different working modes: m = 1 (blue) indicates the mode with '0 s' of UV irradiationtime, m = 2 (orange) indicates the mode with '0 s' and '2 s' of UV irradiation time, m = 3(red) indicates the mode with '0 s', '2 s', and '6 s' of UV irradiation time.

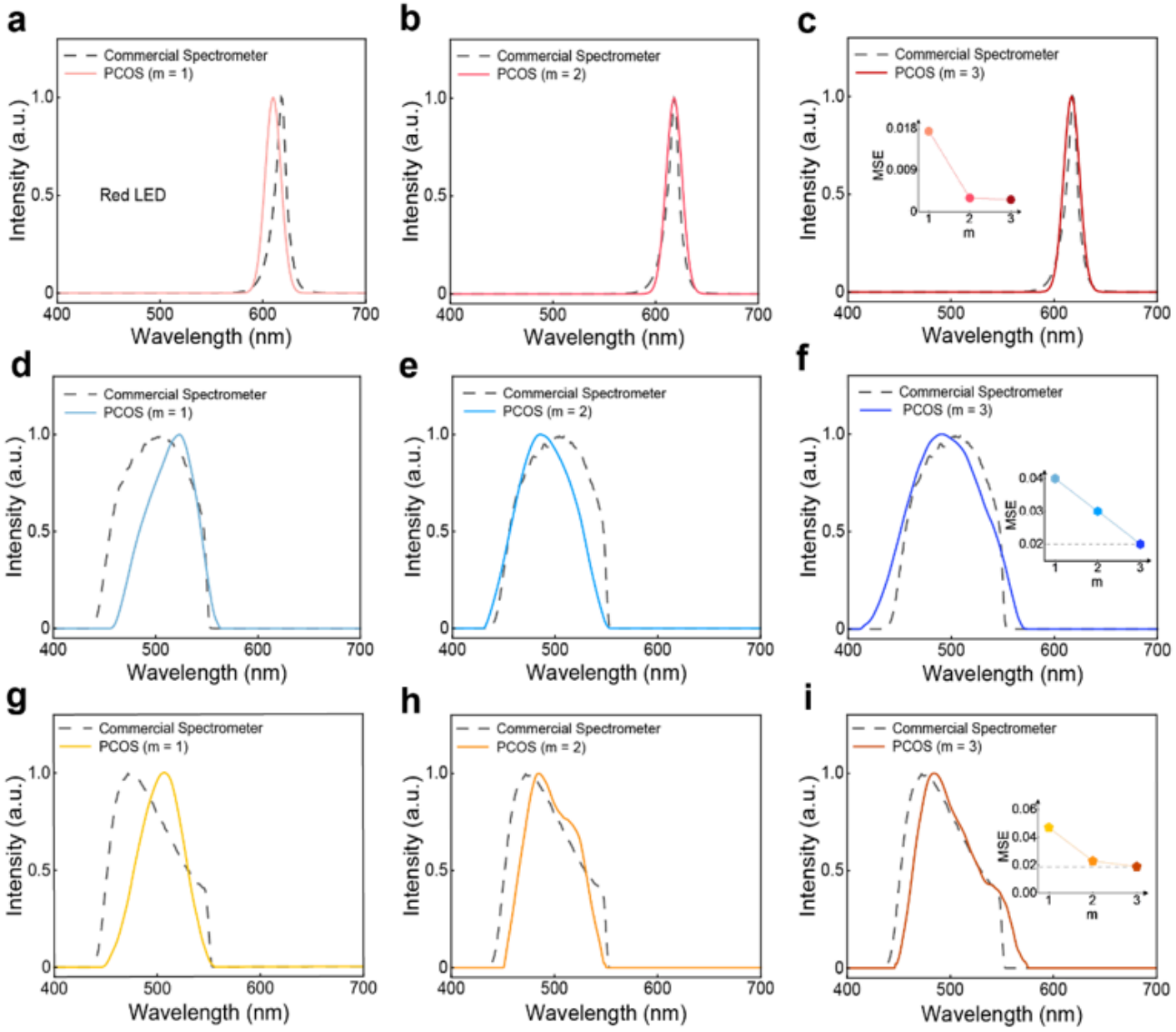


Figure 5

Spectral reconstruction capabilities of narrowbandand broadband spectra under different working modes (m = 1, 2, 3). (a)-(c) Reconstruction of narrow spectra (red LED) based on m = 1, 2, 3 modes, respectively. The inset of (c) shows the MSE of different modes of m. (d-i) Reconstruction of symmetric and asymmetric broadband spectra using 400–550 nm bandpass and color filters. Here, m denotes different working modes: m = 1 (blue) indicates the mode with ‘0 s’ of UV irradiation time, m = 2 (orange) indicates the mode with ‘0 s’ and ‘2 s’ of UV irradiation time, m = 3 (red) indicates the mode with ‘0 s’, ‘2 s’, and ’6 s’ of UV irradiation time.

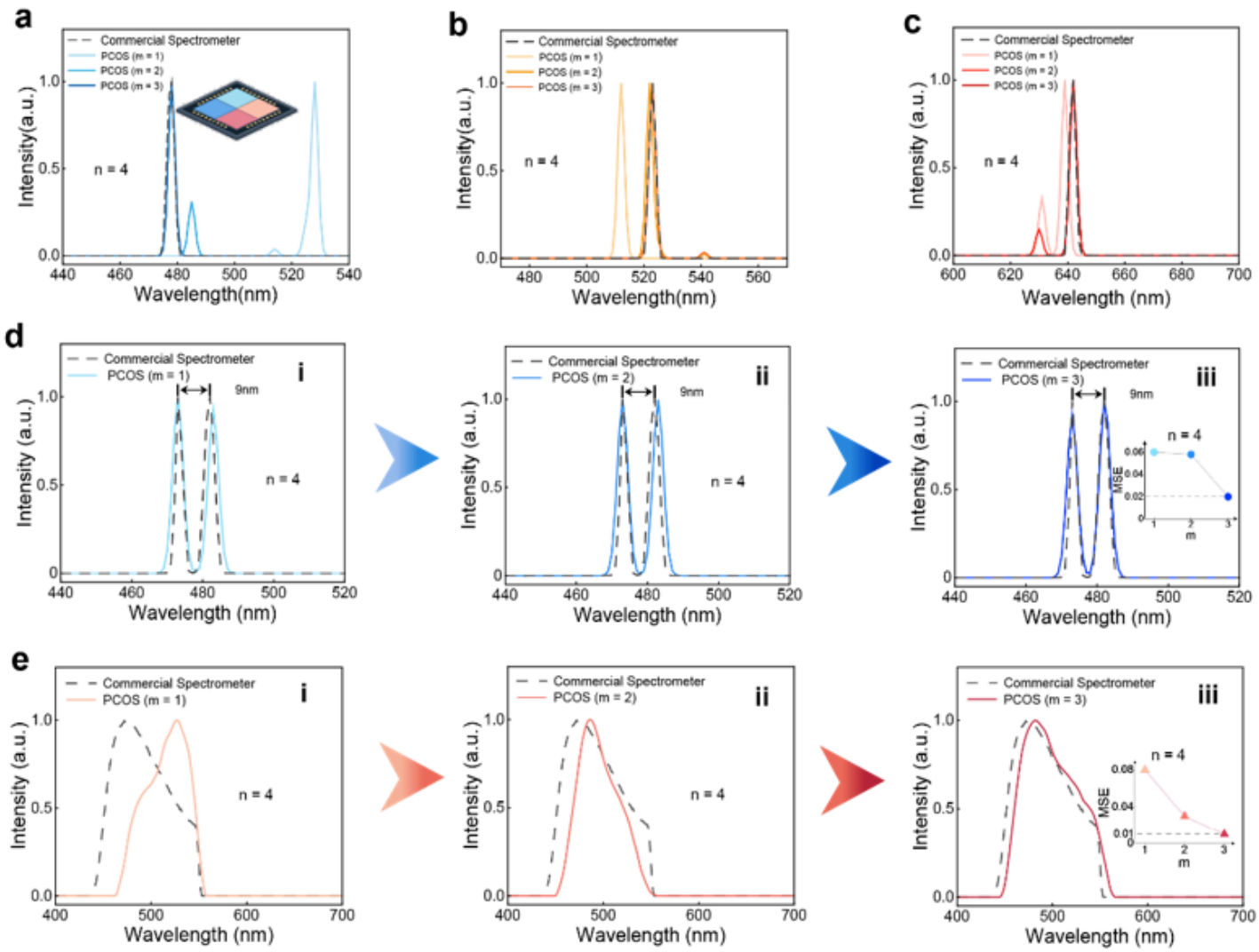


Figure 6

Spectral reconstruction capabilities of PCOS with four filters under different working modes (m = 1, 2, 3). (a-c) The reconstructed spectra of three representative monochromatic lights (peaks at 478 nm, 523 nm, and 642 nm). (d) Reconstruction of the spectrum with two mixed peaks of 9 nm under different working modes. The inset of (d-iii) shows the MSE of different modes of m. (e) Reconstruction of the broadband spectrum generated by a xenon lamp with 400 short-pass and 550 long-pass filters. The inset of (e-iii) shows the MSE of different modes of m. Here, m denotes different working modes: m = 1 (blue) indicates the mode with '0 s' of UV irradiation time, m = 2 (orange) indicates the mode with '0 s' and '2s' of UV irradiation time, m = 3 (red) indicates the mode with '0 s', '2 s ', and '6s' of UV irradiation time.

Supplementary Files

This is a list of supplementary files associated with this preprint. Click to download.

- SupportingInformation.docx